



 Cite this: *RSC Adv.*, 2023, **13**, 2411

# Simultaneous passivation on both A and X sites of halogen perovskite with magnesium benzoate†

 Chenxin Xu,<sup>a</sup> Lujie Liu,<sup>a</sup> Yurong Huang,<sup>b</sup> Fei Zhang<sup>b</sup> and Hui Cao \*<sup>a</sup>

Surface modification engineering is a well-known effective passivation method for making efficient and stable perovskite solar cells (PSCs). However, to our knowledge, little attention has been paid to simultaneously passivating the A and X sites of halogen perovskites. Herein, we introduced an organometallic salt (C<sub>6</sub>H<sub>5</sub>COO)<sub>2</sub>Mg (MgBEN) as a passivator, and as a result, the C<sub>6</sub>H<sub>5</sub>COOMg<sup>+</sup> passivates the A site and C<sub>6</sub>H<sub>5</sub>COO<sup>-</sup> the X site on the perovskite layer, significantly reducing the trap-state density and nonradiative recombination. Moreover, the modification induces the perovskite film quality to improve, which may decrease the charge accumulation and facilitate carrier transport. By optimizing the concentration of the MgBEN, the perovskite film showed an increased grain size (from 1.18 μm to 1.61 μm), and the best device exhibited an enhanced power conversion efficiency (PCE) of 22.24%. Meanwhile, the device after modification performed with good long-term stability.

 Received 26th October 2022  
 Accepted 9th January 2023

DOI: 10.1039/d2ra06761g

[rsc.li/rsc-advances](https://rsc.li/rsc-advances)

## Introduction

Within the past decade, hybrid organic–inorganic metal halide perovskite materials have demonstrated various applications in optoelectronic devices, including photovoltaic,<sup>1,2</sup> photodetectors,<sup>3,4</sup> and light-emitting diodes.<sup>5</sup> Among these, perovskite solar cells show great potential for next-generation photovoltaic technology due to their high light absorption coefficient,<sup>6</sup> excellent carrier diffusion length,<sup>7</sup> tuneable direct bandgap,<sup>8</sup> and cost-efficient fabrication process.<sup>9</sup> Recently, the state-of-the-art conventional n-i-p PSCs have realized 25.7%<sup>10</sup> PCE compared with the original 3.8%.<sup>2</sup> However, there is still considerable room to further boost the PCE of PSCs to reach the Shockley–Queisser limit,<sup>11</sup> and the long-term stability of PSCs under actual operational conditions is still the major obstacle for their commercialization.<sup>12</sup> Therefore, targeted strategies are urgently needed to fabricate efficient and stable solar cells based on hybrid halide perovskite.

Previous studies have shown that metal halide perovskite is extremely sensitive to the surrounding environment, principally including damp,<sup>13</sup> heat,<sup>14</sup> and light,<sup>15</sup> resulting in defects generation and accumulation at the interfaces and the bulk of perovskite. Ultimately, these defects cause non-radiative recombination and instability. For purpose of eliminating these undesirable defects, myriads of approaches have been

adopted to tailor the quality of perovskite films, such as additive engineering,<sup>16</sup> solvent engineering,<sup>17</sup> and interface engineering.<sup>18–20</sup> Among these approaches, modifying interfaces of PSCs has become more pivotal to enhancing device performance.<sup>21</sup>

Numerous passivating methods such as small molecules,<sup>22</sup> alkylammonium halogen salts,<sup>16</sup> and multifunctional molecular modulators,<sup>23</sup> have been developed to fabricate highly efficient and stable PSCs. Wang *et al.*<sup>24</sup> used eco-friendly strontium chloride (SrCl<sub>2</sub>) as surface passivation on A site of perovskite films to suppress ion migration. Recently, Li *et al.*<sup>25</sup> utilized an organometallic compound, ferrocenyl-bis-thiophene-2-carboxylate (FcTc<sub>2</sub>), to modify the B sites at the interface of inverted PSCs. Zou *et al.*<sup>26</sup> reported one pyridine derivative Py-HN<sub>2</sub> to passivate the perovskite film, it can effectively hinder the formation of X site vacancies. However, current surface modification strategies<sup>27,28</sup> focus more on passivating one of these three kinds of defects. It was also reported that synergistic passivation on two sites could achieve better photo-electric conversion of PSCs. Natural small organic dye, indigo,<sup>29</sup> which contains desired carbonyl and amino functional groups, can provide bifunctional chemical passivation on both B and X sites. However, surface modification strategy which could simultaneously passivate A and X sites was seldom reported.

Inspired by previous work about alkaline earth metal,<sup>30</sup> in this work, we introduce an organic metal salt, magnesium benzoate, as a surface passivator. On the one hand, C<sub>6</sub>H<sub>5</sub>COO<sup>-</sup> could fill X site (V<sub>I</sub>), leading to a much stronger interaction with Pb. Meanwhile, the benzene ring exhibits great hydrophobicity by preventing the permeation of moisture.<sup>31</sup> On the other hand, C<sub>6</sub>H<sub>5</sub>COOMg<sup>+</sup> could fill A site (V<sub>FA</sub>). Because Mg<sup>2+</sup> (72 pm) has a smaller ionic radius than FA<sup>+</sup> (256 pm), the Mg–I band is more

<sup>a</sup>School of Chemistry and Materials Science, Nanjing University of Information Science and Technology, Nanjing 210044, People's Republic of China. E-mail: ycaoh@hotmail.com

<sup>b</sup>School of Environmental Science and Engineering, Nanjing University of Information Science and Technology, Nanjing 210044, People's Republic of China

† Electronic supplementary information (ESI) available. See DOI: <https://doi.org/10.1039/d2ra06761g>



likely to be covalent corresponding to Fajan's rule.<sup>32</sup> As a result, the more covalent character of (Mg-I) could effectively donate electrons to Pb, then increase the electron density of Pb.<sup>33</sup> Moreover, we speculate that the  $\pi$ - $\pi$  stack effect between the modification layer and hole transport layer (HTL) may benefit the hole transport and decrease the charge accumulation<sup>34</sup> and non-recombination at the interface. Synergistic passivation of the A site as well as the X site can both improve the efficiency and stability of the device. At last, the champion PCE of MgBEN passivated PSCs is enhanced from 19.94% to 22.24% with simultaneously improved FF,  $V_{OC}$ , and  $J_{SC}$  to 79.33, 1.074 V, and 26.09 mA cm<sup>-2</sup>, respectively. Moreover, the device retained 90% of the original PCE after 30 days of storage in dry air (RH: 20–30%).

## Results and discussion

FAPbI<sub>3</sub> perovskite films were prepared by a one-step method, as displayed in Fig. 1. The devices in this study were fabricated with a mesoporous n-i-p type architecture of fluorine-doped tin oxide (FTO)/compact TiO<sub>2</sub> (c-TiO<sub>2</sub>)/mesoporous TiO<sub>2</sub> (m-TiO<sub>2</sub>)/FAPbI<sub>3</sub> perovskite/(C<sub>6</sub>H<sub>5</sub>COO)<sub>2</sub>Mg-modification/spiro-OMeTAD/Au. To systematically investigate the effects of different concentrations of MgBEN, we set three different concentrations of 0.1, 1, and 5 mM. And the perovskite film with 0 mM MgBEN modification was denoted as the control film. In the experimental section, a detailed description of the fabrication processing was presented.

To explore the influence of various concentrations of MgBEN on the lattice quality of the perovskite film, we utilized X-ray diffraction (XRD) to characterize. Fig. 2a displays the XRD patterns of the perovskite films, we could see two dominant peaks, corresponding to (100) and (200) diffraction indexes, respectively, and no peak was found at about 11.6°, which represents  $\delta$ -phase.<sup>35</sup> Compared to the control film, all concentrations showed an enhanced diffraction intensity at two dominant peaks (no distinct peaks shifted and no additional peaks generated), suggesting the better crystallinity of the perovskite film.<sup>36</sup> The full width at half-maximum (FWHM) of the (100) peak drops from 0.104 to 0.099 after MgBEN modification, as depicted in Fig. S1,† also demonstrating that the

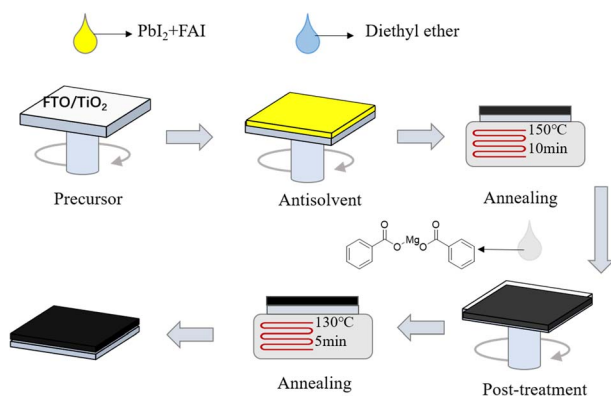


Fig. 1 Schematic diagram of perovskite solar cell preparation process.

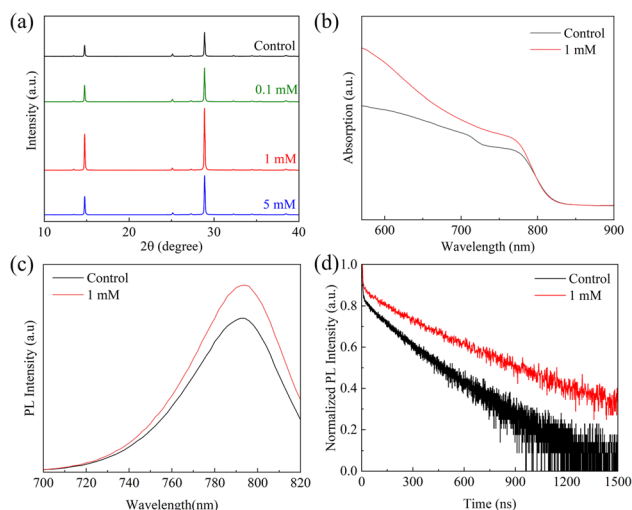


Fig. 2 (a) The XRD patterns, (b) UV-vis absorption spectra, (c) the steady PL spectra, and (d) the TRPL spectra of the control and 1 mM MgBEN-modified perovskite films.

modification validly improves the crystallinity of perovskite.<sup>31</sup> The better the crystallinity of the film, the fewer nonradiative charge recombination centers, this is conducive to boosting  $V_{OC}$ .<sup>37</sup> Lattice strain was strictly correlated with the augmented non-radiative recombination and defect concentration, which contributes detrimentally to device performance.<sup>38–40</sup> Using Williamson–Hall (WH) plots (individual plots for different concentrations are shown in Fig. S2†), it was found that the lattice strain of the perovskite films decreased with the 1 mM MgBEN modification, which is accountable for the reduced nonradiative recombination and enhanced carrier lifetime.<sup>35</sup>

In Fig. 2b, the Ultraviolet-visible (UV-vis) absorption spectra of the 1 mM MgBEN-modified and control perovskite films were used to further analyse the difference of light absorption properties (absorption spectra of other concentrations treated perovskite films as depicted in Fig. S3†). Obviously, after modification, the film showed the higher absorption over the entire wavelength compared to the control film with similar absorption edges. The enhanced absorbance after modification is mainly due to the formation of better perovskite film.<sup>41,42</sup> Furthermore, as shown in Fig. S4,† we used Tauc plot to calculate the optical bandgap of control and MgBEN-modified perovskite films. We found that the bandgap was increased from 1.514 eV to 1.519 eV. However, the  $J_{SC}$  did not become smaller, but larger. Thus, the increase in  $J_{SC}$  may be due to a reduction in charge accumulation, which promotes carrier transport and then reduces the non-radiative recombination.

To investigate the influence of MgBEN modification on the charge carrier dynamics and recombination, we measured the steady-state photoluminescence (PL) and time-resolved photoluminescence (TRPL). Fig. 2c shows that the PL intensity of the MgBEN-modified film is stronger than the control film, which signifies the decrease of trapping centers and the suppression of nonradiative recombination<sup>43</sup> after the modification. As shown in Fig. 2d, the corresponding TRPL spectra of control



and MgBEN-modified perovskite films were fitted with a bi-exponential equation<sup>44</sup>

$$y = A_1 \exp\left(-\frac{t}{\tau_1}\right) + A_2 \exp\left(-\frac{t}{\tau_2}\right) \quad (1)$$

where  $A_1$  and  $A_2$  denote the decay amplitudes,  $\tau_1$  and  $\tau_2$  represent the fast and slow decay time. Other concentrations of PL and TRPL are shown in Fig. S5.† The average carrier lifetime can be estimated by the following equation<sup>45</sup>

$$\tau_{\text{ave}} = \frac{A_1 \tau_1^2 + A_2 \tau_2^2}{A_1 \tau_1 + A_2 \tau_2} \quad (2)$$

The fitted parameters are presented in Table 1. Compared with the control perovskite film ( $\tau_{\text{ave}} = 157.43$  ns), the MgBEN-modified perovskite film displays a longer average carrier lifetime of 288.94 ns. Meanwhile, the  $\tau_{\text{ave}}$  of films treated by the other concentrations also increases (see Table S1†). The elongated lifetime demonstrates that the modification of MgBEN can significantly inhibit nonradiative recombination, consistent with the above WH plots analysis.

We measured scanning electron microscopy (SEM) images of perovskite films to investigate the MgBEN-modified perovskite films' surface morphology. Fig. 3a and b display top-view SEM images of the control FAPbI<sub>3</sub> films and with 1 mM MgBEN modification films. Compared to the control perovskite film, the modified film displays a better morphology with clearly increase in grain size. To quantitatively analyse the change in

**Table 1** TRPL parameters of control and 1 mM MgBEN-modified perovskite films

	$A_1$ (%)	$\tau_1$ (ns)	$A_2$ (%)	$\tau_2$ (ns)	$\tau_{\text{ave}}$ (ns)
Control	71.09	1.62	28.91	161.28	157.43
1 mM	56.72	3.40	43.28	293.28	288.94

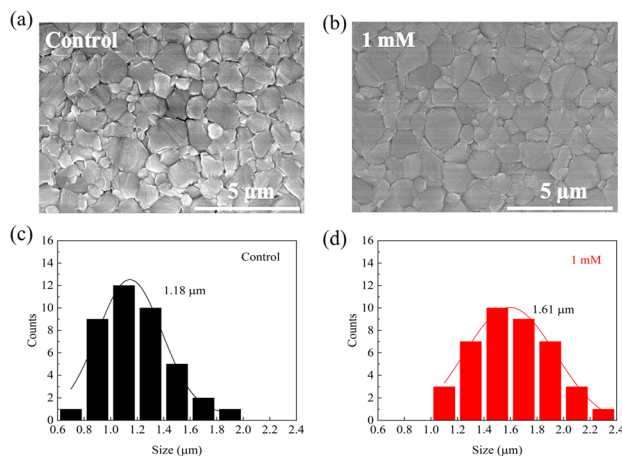


**Fig. 3** Top-view SEM images of (a) the control and (b) 1 mM MgBEN-modified perovskite films, and histograms of grain size distributions of (c) the control and (d) 1 mM MgBEN-modified perovskite films, respectively.

the grain size, the average size was calculated based on the SEM images. The distribution visually illustrates that the average grain size increased from 1.18  $\mu\text{m}$  to 1.61  $\mu\text{m}$ , and the maximum grain size of MgBEN-modified film was up to 2.3  $\mu\text{m}$ , as shown in the Fig. 3c and d. The above results prove that the modification of MgBEN can effectively improve the quality of perovskite film, this is favourable for the photovoltaic performances and stability of the solar cells.<sup>37</sup> Images and size distribution modified by other concentrations are shown in Fig. S6.† When the observed scale is 1  $\mu\text{m}$ , we found that the grains of the 1 mM MgBEN-modified film were more closely connected, which may suppress the non-radiative recombination at the grain boundaries and facilitate the carrier transport. Corresponding SEM images are shown in Fig. S7.† As depicted in Fig. S8,† we tested the EDS of the MgBEN-modified films and found a small amount of Mg, indicating that MgBEN was effectively attached to the perovskite films. To verify whether the MgBEN surface modification affects the thickness of the perovskite layer, we made a perovskite cross-section based on the TiO<sub>2</sub> layer and found that the thickness of the perovskite layer did not change significantly. As shown in Fig. S9.†

To understand the effect of the MgBEN modification on photovoltaic performance, we fabricated devices with the abovementioned structure in the air with 30–45% humidity, as shown in Fig. 4a. Fig. 4b displays the typical current–voltage ( $J$ – $V$ ) curves of the devices treated with different concentrations of MgBEN, and the respective photovoltaic parameters are summarized in Table 2. Obviously, the photovoltaic performances increased after being modified by MgBEN. Notably, the champion device obtained a maximum PCE of 22.24% under 1 mM MgBEN concentration, with a FF of 79.33%, a  $V_{\text{OC}}$  of 1.07 V, and a  $J_{\text{SC}}$  of 26.09  $\text{mA cm}^{-2}$ . The control device exhibited a PCE of 19.94%, a FF of 79.25%, a  $V_{\text{OC}}$  of 1.01 V, and a  $J_{\text{SC}}$  of 24.80  $\text{mA cm}^{-2}$ . We found that, apart from enhanced  $V_{\text{OC}}$ , the increased PCE of devices was mainly attributed to better  $J_{\text{SC}}$ ,

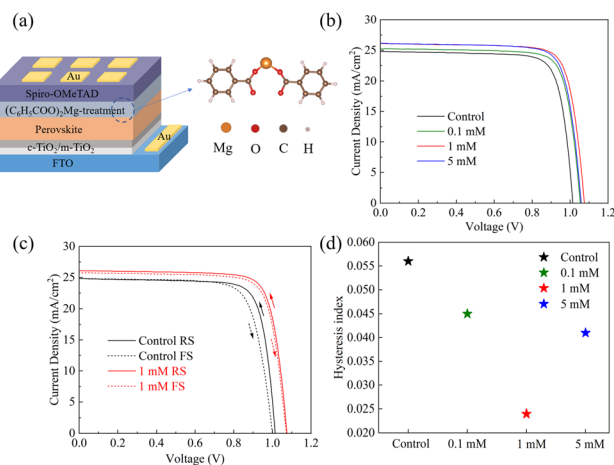


**Fig. 4** (a) Device structure with MgBEN modification, (b)  $J$ – $V$  curves of the devices based on control and different concentrations of MgBEN modification, (c)  $J$ – $V$  curves of the champion cells (control and 1 mM MgBEN modification), and (d) hysteresis index of different concentrations of MgBEN modification.



Table 2 Hysteresis measurements of PSCs at different concentrations of MgBEN modification

Samples	Scan direction	$V_{OC}$ (V)	$J_{SC}$ ( $\text{mA cm}^{-2}$ )	FF (%)	PCE (%)	HI
Control	Forward	1.00	24.81	75.93	18.83	0.056
	Reverse	1.01	24.80	79.25	19.94	
0.1 mM	Forward	1.02	25.23	78.23	20.18	0.045
	Reverse	1.05	25.24	79.46	21.13	
1 mM	Forward	1.07	25.75	78.65	21.71	0.024
	Reverse	1.07	26.09	79.33	22.24	
5 mM	Forward	1.05	25.13	79.38	20.94	0.041
	Reverse	1.06	26.10	79.11	21.84	

probably due to the modified perovskite film becoming more conductive to charge carriers.<sup>46</sup>

Meanwhile, the hysteresis was an important issue in the PSCs, it was related to the ion migration and trap states, and the hysteresis index (HI) of the device was calculated according to the following equation<sup>47</sup>

$$HI = \frac{PCE_{\text{reverse}} - PCE_{\text{forward}}}{PCE_{\text{reverse}}} \quad (3)$$

Here, the hysteresis characteristics were obtained by using different scan directions (reverse scanning (RS), forward scanning (FS)), and the results were depicted in Fig. 4c. Table 2 and Fig. 4d demonstrate that HI values depend on the scan direction. We found that the HI values of MgBEN-modified devices significantly reduced from 0.056 (for the control device) to 0.024, suggesting better carrier transport and collection which accounted for the synergistic effect of defect passivation and grain size increase.<sup>48</sup>

In order to avoid experimental contingency, we tested 20 sets of data for each simple. Fig. 5 displays the statistical  $J_{SC}$ ,  $V_{OC}$ , FF, and PCE for the control and different concentrations of MgBEN. We found that the modification of 1 mM MgBEN substantially improves  $V_{OC}$  and  $J_{SC}$ , leading to a better PCE. Compared to the

control and other concentrations, the data of 1 mM MgBEN modification has smaller dispersion of photovoltaic parameters of  $V_{OC}$  and FF, and relatively smaller  $J_{SC}$ . Although PCE has the largest dispersion, its minimum is the highest, which also indicates that 1 mM MgBEN has a better modification effect than control and other concentrations.

We suggested a probable mechanism for the passivation of FAPbI<sub>3</sub> surface defects by MgBEN in Fig. 6 and explained as follows:  $\text{C}_6\text{H}_5\text{COOMg}^+$  could fill A site ( $V_{FA}$ ), meanwhile, it can form a more likely covalent with  $\text{I}^-$ , which can effectively prevent the migration of cations at the A site. Based on previous studies,<sup>49</sup> compared to  $\text{Cl}^-$ ,  $\text{Br}^-$ ,  $\text{I}^-$  and  $\text{BF}_4^-$ ,  $\text{HCOO}^-$  has the highest binding energy to  $\text{I}^-$  vacant sites.  $\text{C}_6\text{H}_5\text{COO}^-$ , the homologue of  $\text{HCOO}^-$  was introduced here, allowing for the similar passivation of the X sites.

At present, stability is still a major challenge for the commercialization of PSCs.<sup>50</sup> To confirm the influence of the MgBEN modification on the stability of perovskite, we tracked the long-term stability of devices stored in dry air (RH: 20–30%). As shown in Fig. 7a, compared to the control, in the 30 days test, the modified MgBEN still exceeded 90% of the original PCE. In addition to this, steady-state PL spectra were measured every ten minutes to investigate the stability of perovskite films. As depicted in Fig. 7c, the PL intensity of MgBEN-modified perovskite film remained virtually unchanged, and only decayed slightly during the first 10 minutes. In contrast, the PL intensity of the control perovskite film, as shown in Fig. 7b, experienced a significant decay within 50 minutes. This indicates that nonradiative recombination is significantly suppressed, suggesting a remarkably reduced trap state in the MgBEN-modified perovskite film.

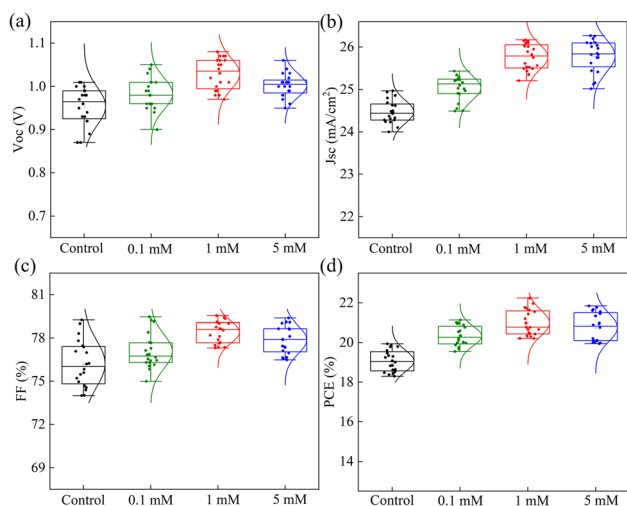


Fig. 5 Statistical photovoltaic parameters of (a)  $V_{OC}$ , (b)  $J_{SC}$ , (c) FF, and (d) PCE.

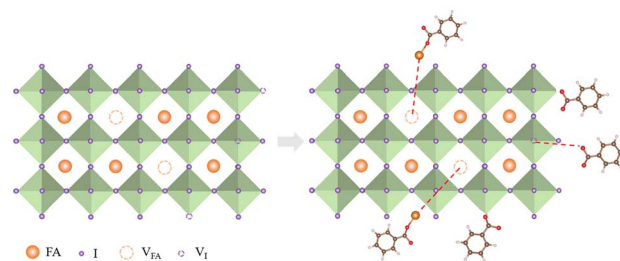


Fig. 6 Mechanism diagram of synergistic passivation of A and X sites by MgBEN on the surface of perovskite films.





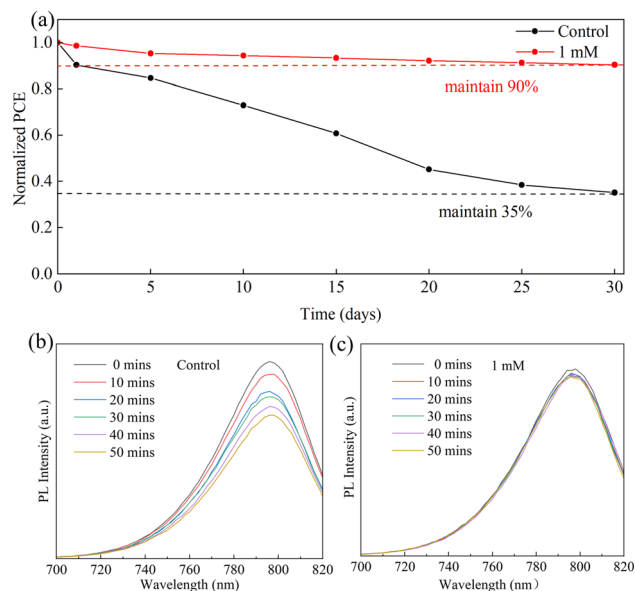


Fig. 7 Device stability measured at room temperature in dry air with 30–40% humidity within 30 days (a). And variations in photoluminescence were tested every ten mins within 50 min of the control perovskite film (b) and that of 1 mM MgBEN-modified perovskite film (c).

## Conclusions

In short, we have demonstrated a simple defect passivation method by passivating MgBEN on perovskite film. We found that the MgBEN treatment increased grain size, improved the film quality and decreased lattice strain, contributing to the enhanced carrier transport and reduction of non-radiative recombination. The champion device prepared with MgBEN passivation obtained a PCE of 22.24% with negligible hysteresis due to the synergistic passivation of the A and X sites. More importantly, the MgBEN modification remarkably increased the perovskite film stability. The corresponding PSCs preserved nearly 90% of the original PCE, while the PCE of the untreated devices kept only 35% of the initial within 30 days (RH: 20–30%). Our study offers a new strategy to fabricate highly efficient and stable PSCs.

## Experimental

### Materials

Titanium(diisopropoxide) bis(2,4-pentanedionate) (75%, Macklin), *n*-Butanol (99.8%, Aladdin). Methylammonium chloride (MAcI, 99.5%), formamidinium iodide (FAI), lead iodide (PbI<sub>2</sub>), spiro-OMeTAD, Li-TFSI, FK209 were purchased from Xi'an p-OLED. chlorobenzene (CB), 4-*tert*-butyl pyridine (tBP). Magnesium benzoate ((C<sub>6</sub>H<sub>5</sub>COO)<sub>2</sub>Mg) were purchased from Sigma-Aldrich. Dimethyl sulfoxide (DMSO) (99.9% Macklin) and dimethylformamide (DMF) (99.9%, Macklin).

### Device fabrication

FTO substrates were treated by deionized water, decon90, isopropanol, ethyl alcohol, and deionized water three times for

20 min sequentially. Then, they were dried in an oven at 100 °C and treated with 30 min ultraviolet ozone. The compact titanium dioxide layer (*c*-TiO<sub>2</sub>), was spin-coated using diisopropoxy bis(acetylacetonate) titanium solution into *n*-butanol (1 : 16, V/V) at 2000 rpm for 45 s and annealed in an oven at 120 °C for 15 min. After cooled down, the mesoscopic TiO<sub>2</sub> layer (*m*-TiO<sub>2</sub>) was spin-coated at 5000 rpm for 10 s and calcined at 500 °C for 60 min. The mesoscopic TiO<sub>2</sub> solution needs to prepare 24 hours in advance, diluted TiO<sub>2</sub> paste with ethanol, mass ratio of 1 : 8.

In an N<sub>2</sub> glove box, perovskite precursor solution was obtained with PbI<sub>2</sub> and FAI and MAcI in a mixture of DMSO and DMF solvents (molar ratio of DMF/DMSO = 4 : 1). Then, the FAPbI<sub>3</sub> solution was coated on the *m*-TiO<sub>2</sub> substrate and spined at 1000 rpm for 18 s and 4000 rpm for 28 s. In the second stage of the spin-coating (high speed) process, the antisolvent (1 ml of diethyl ether) was dumped on the substrate after the first 8 s, then after 20 seconds of vacuum treatment in a chamber with a pressure of less than 0.1 Pa, the substrate was transferred to a hot plate at 150 °C for 10 min with 35–45% humidity ambient conditions. Mg(C<sub>6</sub>H<sub>5</sub>COO)<sub>2</sub> was dissolved in ethyl alcohol, then 100 μL solution spin-coated on the substrate at 3000 rpm for 10 s, subsequently annealed at 130 °C for 5 min. After the films cooling down to room temperature, 40 μL Spiro-OMeTAD solution was spin-coated on the substrate at 3000 rpm for 30 s. Finally, 80 nm gold electrode was deposited on the substrate by thermal vacuum evaporation.

### Characterization

The PL and TRPL spectra (PicoQuant GmbH, FluTime 300) were obtained by time-single setting under an excitation source at 650 nm. XRD spectra were recorded with a scan range of 10–50° for 5° per minute. The UV-Vis absorption spectra (UV-3600) were measured from 300 to 900 nm. The perovskite film surface was examined by SEM (HITACHI, S-4800) to investigate grain size, then analyzed surface elemental content by EDS. The grain size contribution of perovskite was analyzed by Nano measurer 1.2 software. A solar simulator (Sol3A Newport) was used to capture the *J*-*V* curves of the PSCs. The source was equipped with a xenon lamp (450 W) that simulated AM 1.5 G of sunlight with an optical density of 100 mW cm<sup>-1-2</sup>, calibrated by using a standard silicon cell.

## Conflicts of interest

There are no conflicts to declare.

## Acknowledgements

This work was supported by Nanxin Pharm Co., Ltd, Nanjing.

## Notes and references

- H. S. Kim, C. R. Lee, J. H. Im, K. B. Lee, T. Moehl, A. Marchioro, S. J. Moon, R. Humphry-Baker, J. H. Yum, J. E. Moser, M. Grätzel and N. G. Park, *Sci. Rep.*, 2012, 2, 591.



- 2 A. Kojima, K. Teshima, Y. Shirai and T. Miyasaka, *J. Am. Chem. Soc.*, 2009, **131**, 6050–6051.
- 3 Y. Wang, D. Yang, X. Zhou, S. M. Alshehri, T. Ahamad, A. Vadim and D. Ma, *J. Mater. Chem. C*, 2016, **4**, 7415–7419.
- 4 H. Zhang, Y. Xiao, F. Qi, P. Liu, Y. Wang, F. Li, C. Wang, G. Fang and X. Zhao, *ACS Sustainable Chem. Eng.*, 2019, **7**, 8236–8244.
- 5 Z. Shi, Y. Li, S. Li, X. Li, D. Wu, T. Xu, Y. Tian, Y. Chen, Y. Zhang, B. Zhang, C. Shan and G. Du, *Adv. Funct. Mater.*, 2018, **28**, 1707031.
- 6 J. Huang, Y. Yuan, Y. Shao and Y. Yan, *Nat. Rev. Mater.*, 2017, **2**, 17042.
- 7 H. D. Pham, L. Xianqiang, W. Li, S. Manzhos, A. K. K. Kyaw and P. Sonar, *Energy Environ. Sci.*, 2019, **12**, 1177–1209.
- 8 D. B. Khadka, Y. Shirai, M. Yanagida, T. Noda and K. Miyano, *ACS Appl. Mater. Interfaces*, 2018, **10**, 22074–22082.
- 9 E. J. Juarez-Perez and M. Haro, *Science*, 2020, **368**, 1309.
- 10 <https://www.nrel.gov/pv/cell-efficiency.html>, accessed on October 20, 2022.
- 11 J. Chen and N.-G. Park, *Adv. Mater.*, 2019, **31**, 1803019.
- 12 N. Li, X. Niu, Q. Chen and H. Zhou, *Chem. Soc. Rev.*, 2020, **49**, 8235–8286.
- 13 S.-W. Kim, G. Kim, C. S. Moon, T.-Y. Yang and J. Seo, *Small Methods*, 2021, **5**, 2001248.
- 14 B. Li, V. Ferguson, S. R. P. Silva and W. Zhang, *Adv. Mater. Interfaces*, 2018, **5**, 1800326.
- 15 H. Xu, Y. Miao, N. Wei, H. Chen, Z. Qin, X. Liu, X. Wang, Y. Qi, T. Zhang and Y. Zhao, *Adv. Energy Mater.*, 2021, **12**, 2103151.
- 16 J. Jeong, M. Kim, J. Seo, H. Lu, P. Ahlawat, A. Mishra, Y. Yang, M. A. Hope, F. T. Eickemeyer, M. Kim, Y. J. Yoon, I. W. Choi, B. P. Darwich, S. J. Choi, Y. Jo, J. H. Lee, B. Walker, S. M. Zakeeruddin, L. Emsley, U. Rothlisberger, A. Hagfeldt, D. S. Kim, M. Gratzel and J. Y. Kim, *Nature*, 2021, **592**, 381–385.
- 17 W. Hui, L. Chao, H. Lu, F. Xia, Q. Wei, Z. Su, T. Niu, L. Tao, B. Du, D. Li, Y. Wang, H. Dong, S. Zuo, B. Li, W. Shi, X. Ran, P. Li, H. Zhang, Z. Wu, C. Ran, L. Song, G. Xing, X. Gao, J. Zhang, Y. Xia, Y. Chen and W. Huang, *Science*, 2021, **371**, 1359–1364.
- 18 Q. Jiang, Y. Zhao, X. Zhang, X. Yang, Y. Chen, Z. Chu, Q. Ye, X. Li, Z. Yin and J. You, *Nat. Photonics*, 2019, **13**, 460–466.
- 19 Z. Xiong, X. Chen, B. Zhang, G. O. Odunmbaku, Z. Ou, B. Guo, K. Yang, Z. Kan, S. Lu, S. Chen, N. A. N. Ouedraogo, Y. Cho, C. Yang, J. Chen and K. Sun, *Adv. Mater.*, 2022, **34**, e2106118.
- 20 Q. Zhuang, C. Zhang, C. Gong, H. Li, H. Li, Z. Zhang, H. Yang, J. Chen and Z. Zang, *Nano Energy*, 2022, **102**, 107747.
- 21 X. Wu, B. Li, Z. Zhu, C. C. Chueh and A. K. Jen, *Chem. Soc. Rev.*, 2021, **50**, 13090–13128.
- 22 Z. Cheng, C. Gao, J. Song, D. Ding, Y. Chen, J. Wang, D. Zhang, L. Chen, X. Wang, Z. Yang, F. Liu, H. Liu and W. Shen, *ACS Appl. Mater. Interfaces*, 2021, **13**, 40778–40787.
- 23 Z. Liu, F. Cao, M. Wang, M. Wang and L. Li, *Angew. Chem., Int. Ed.*, 2020, **59**, 4161–4167.
- 24 S. Wang, H. Cao, X. Liu, Y. Liu, T. Tao, J. Sun and M. Zhang, *ACS Appl. Mater. Interfaces*, 2020, **12**, 3661–3669.
- 25 Z. Li, B. Li, X. Wu, S. A. Sheppard, S. Zhang, D. Gao, N. J. Long and Z. Zhu, *Science*, 2022, **376**, 416–420.
- 26 K. Zou, Q. Li, J. Fan, H. Tang, L. Chen, S. Tao, T. Xu and W. Huang, *ACS Mater. Lett.*, 2022, **4**, 1101–1111.
- 27 W. Zhang, L. He, Y. Meng, H. Kanda, D. Tang, B. Ding, Y. Ding, M. K. Nazeeruddin and X. Li, *Adv. Energy Mater.*, 2022, **12**, 2202189.
- 28 N. Ma, J. Jiang, G. Wang, D. Wang, Y. Zhang, Y. Wang, Y. Wang, Y. Ji, W. Wei and L. Shen, *ACS Appl. Mater. Interfaces*, 2021, **13**, 44401–44408.
- 29 J. Guo, J. Sun, L. Hu, S. Fang, X. Ling, X. Zhang, Y. Wang, H. Huang, C. Han, C. Cazorla, Y. Yang, D. Chu, T. Wu, J. Yuan and W. Ma, *Adv. Energy Mater.*, 2022, **12**, 2200537.
- 30 Y. Liu, H. Cao, X. Liu, R. Zhu, T. Tao and J. J. N. Sun, *Nanotechnology*, 2021, **32**, 355201.
- 31 Z. Liu, F. Cao, M. Wang, M. Wang and L. Li, *Angew. Chem., Int. Ed.*, 2020, **59**, 4161–4167.
- 32 K. Fajans, Struktur und Deformation der Elektronenhüllen in ihrer Bedeutung für die chemischen und optischen Eigenschaften anorganischer Verbindungen, *Naturwissenschaften*, 1923, **11**, 165–172.
- 33 M. Lyu, D.-K. Lee and N.-G. J. N. H. Park, *Nanoscale Horiz.*, 2020, **5**, 1332–1343.
- 34 A. R. b. Mohd Yusoff, M. Vasilopoulou, D. G. Georgiadou, L. C. Palilis, A. Abate and M. K. Nazeeruddin, *Energy Environ. Sci.*, 2021, **14**, 2906–2953.
- 35 G. Kim, H. Min, K. S. Lee, D. Y. Lee, S. M. Yoon and S. I. Seok, *Science*, 2020, **370**, 108–112.
- 36 H. Zheng, G. Liu, W. Wu, H. Xu and X. Pan, *ChemSusChem*, 2021, **14**, 3147–3154.
- 37 R. Zhao, T. Wu, R. Zhuang, Y. Hua and Y. Wang, *Energy Environ. Mater.*, 2022, e12417.
- 38 T. W. Jones, A. Oshero, M. Alsari, M. Sponseller, B. C. Duck, Y.-K. Jung, C. Settens, F. Niroui, R. Brenes, C. V. Stan, Y. Li, M. Abdi-Jalebi, N. Tamura, J. E. Macdonald, M. Burghammer, R. H. Friend, V. Bulović, A. Walsh, G. J. Wilson, S. Lilliu and S. D. Stranks, *Energy Environ. Sci.*, 2019, **12**, 596–606.
- 39 D.-J. Xue, Y. Hou, S.-C. Liu, M. Wei, B. Chen, Z. Huang, Z. Li, B. Sun, A. H. Proppe, Y. Dong, M. I. Saidaminov, S. O. Kelley, J.-S. Hu and E. H. Sargent, *Nat. Commun.*, 2020, **11**, 1514.
- 40 C. Zhu, X. Niu, Y. Fu, N. Li, C. Hu, Y. Chen, X. He, G. Na, P. Liu, H. Zai, Y. Ge, Y. Lu, X. Ke, Y. Bai, S. Yang, P. Chen, Y. Li, M. Sui, L. Zhang, H. Zhou and Q. Chen, *Nat. Commun.*, 2019, **10**, 1–11.
- 41 C. Liu, S. Liu, Y. Wang, Y. Chu, K. Yang, X. Wang, C. Gao, Q. Wang, J. Du, S. Li, Y. Hu, Y. Rong, L. Guo, A. Mei and H. Han, *Adv. Funct. Mater.*, 2021, **31**, 2010603.
- 42 G. Liu, H. Zheng, J. Ye, S. Xu, L. Zhang, H. Xu, Z. Liang, X. Chen and X. Pan, *ACS Energy Lett.*, 2021, **6**, 4395–4404.
- 43 Q. Zhou, Y. Gao, C. Cai, Z. Zhang, J. Xu, Z. Yuan and P. Gao, *Angew. Chem., Int. Ed.*, 2021, **60**, 8303.
- 44 J. Chen, X. Zhao, S.-G. Kim and N.-G. Park, *Adv. Mater.*, 2019, **31**, 1902902.



## Paper

- 45 J. Chen, S.-G. Kim and N.-G. Park, *Adv. Mater.*, 2018, **30**, 1801948.
- 46 W. Sun, M. Zhang, S. Wang, F. Cao, J. Zou, Y. Du, Z. Lan and J. Wu, *J. Mater. Chem. C*, 2021, **9**, 7726–7733.
- 47 W. Li, M. U. Rothmann, Y. Zhu, W. Chen, C. Yang, Y. Yuan, Y. Y. Choo, X. Wen, Y.-B. Cheng, U. Bach and J. Etheridge, *Nat. Energy*, 2021, **6**, 624–632.
- 48 G. Xia, B. Huang, Y. Zhang, X. Zhao, C. Wang, C. Jia, J. Zhao, W. Chen and J. Li, *Adv. Mater.*, 2019, **31**, 1902870.
- 49 J. Jeong, M. Kim, J. Seo, H. Lu, P. Ahlawat, A. Mishra, Y. Yang, M. A. Hope, F. T. Eickemeyer, M. Kim, Y. J. Yoon, I. W. Choi, B. P. Darwich, S. J. Choi, Y. Jo, J. H. Lee, B. Walker, S. M. Zakeeruddin, L. Emsley, U. Rothlisberger, A. Hagfeldt, D. S. Kim, M. Grätzel and J. Y. Kim, *Nature*, 2021, **592**, 381–385.
- 50 G. Nazir, S.-Y. Lee, J.-H. Lee, A. Rehman, J.-K. Lee, S. I. Seok and S.-J. Park, *Adv. Mater.*, 2022, **34**, 2204380.

